The Effects of Acoustic Mismatch on Internal Dielectrically Transduced Micromechanical Resonators

Eugene Hwang and Sunil A. Bhave
Electrical and Computer Engineering
Cornell University
Ithaca, NY USA
eoh3@cornell.edu

***Abstract* —This paper presents a supplement to the theory of internal dielectric transduction presented in [1] by including the effects of acoustic mismatch on the resonant frequency and motional impedance of internal dielectrically transduced micromechanical resonators. Analytical expressions for the mode shapes in said resonators are mathematically derived and verified for various dielectric and resonator body materials by comparing numerical simulation results in MATLAB with finite element analysis (FEA) results using COMSOL. Correction factors for mismatched materials are presented to aid in the precise and optimal design of internal dielectrically transduced micromechanical resonators for applications up to tens of gigahertz.**

I. Introduction

Recent progress in the area of RF MEMS resonators has pushed operating frequencies into the gigahertz range while steadily lowering the motional impedance through various design techniques, including large scale resonator arrays and the use of piezoelectric transduction [2], [3]. Such resonators present the possibility for high-Q, integrated filters and low phase noise, monolithic frequency references. Recently, it has been shown in [1] that optimal transduction of an internal dielectrically transduced resonator scales favorably with increasing frequency up to tens of gigahertz, demonstrating the potential for low impedance silicon micromechanical resonators at millimeter-wave frequencies. In fact, such transduction methods are used in [4] to demonstrate both the highest fQ product and the highest resonant frequency ever reported in an electrostatically transduced polysilicon resonator to date.

One obstacle to the wide scale adoption of such devices is the absence of reliable modeling. For simplicity, most micromechanical devices are modeled by simple 1-D theoretical models. This results in discrepancy between the experimental and predicted behavior of these resonators. The reasons for this discrepancy can be largely divided into systematic (e.g., lateral inertia effects) and random sources (e.g., process variations). In this paper, we focus on analytical modeling of internal dielectrically transduced resonators. In particular, the use of a solid transduction dielectric film introduces a predictable source of discrepancy that arises from the acoustic mismatch between the resonator body and the dielectric film. This paper quantifies the effects of acoustic mismatch on resonator properties and allows for the precise and optimal design of internal dielectrically transduced micromechanical resonators.

In section II, we set up the equations of motion for the composite resonator with three distinct regions and derive analytical expressions for the mode shape. In section III, we present numerical simulation results of our theory. In this section, we also discuss, based on the results of these simulations, the impact of acoustic mismatch on the characteristics of the internal dielectrically transduced resonator. Finally, we present correction factors that can be used by the designer to accurately predict the behavior of such resonators.

II. Composite Bar Resonator Theory

Here, we develop the theory for an electrostatically transduced composite bar resonator. The structure is actuated by the capacitive force across the dielectric transducer. This yields a force distribution represented by two delta functions at the interfaces between the dielectric and resonator structure. These forcing functions are equal in magnitude but opposite in direction. Due to the complexity of the full analysis, we make a few simplifying assumptions to aid in the development of this theory. First, we assume zero displacement at the center, i.e., the center is tethered. Also,

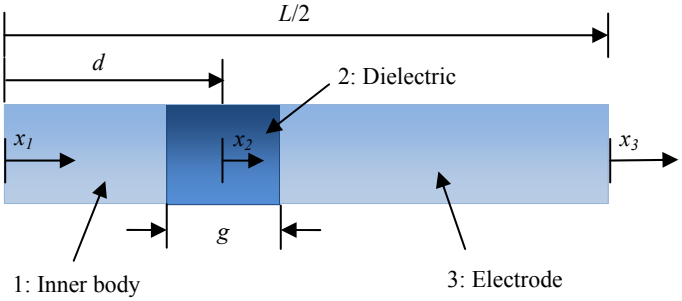

Figure 1. Cross-section of composite resonator geometry and coordinate system

we assume a symmetric structure and mode shape about the center, allowing consideration of only half the resonator. And finally, we assume only 1-D longitudinal motion. Note that this theory is only applicable to bar resonators, but gives insight into the general effects of acoustic mismatch in similar composite bulk-mode devices like those in [5], [6].

The analysis begins by first dividing half of the resonator into three sections: the inner body, the dielectric film, and the electrode. These sections will be denoted in subsequent equations by subscripts 1, 2, and 3, respectively. Fig. 1 indicates the initial coordinate systems used in each region to simplify the analysis. This analysis utilizes linearity to find the overall response of the system as the sum of impulse responses arising from excitations at each dielectric interface. The three coupled wave equations are given in (1)-(3).

$$\left[\rho_{diel}\frac{\partial^2}{\partial t^2}-b_{si}\frac{\partial^3}{\partial t\partial {x_1}^2}-E_{si}\frac{\partial^2}{\partial {x_1}^2}\right]U_1(x_1\mid\zeta_1)e^{-j\omega t}=\delta(x_1-\zeta_1)e^{-j\omega t} \tag{1}$$

$$\left[\rho_{diel}\frac{\partial^2}{\partial t^2}-b_{diel}\frac{\partial^3}{\partial t\partial {x_2}^2}-E_{diel}\frac{\partial^2}{\partial {x_2}^2}\right]U_2(x_2\mid\zeta_2)e^{-j\omega t}=\delta(x_2-\zeta_2)e^{-j\omega t} \tag{2}$$

$$\left[\rho_{si}\frac{\partial^2}{\partial t^2}-b_{si}\frac{\partial^3}{\partial t\partial {x_3}^2}-E_{si}\frac{\partial^2}{\partial {x_3}^2}\right]U_3(x_3\mid\zeta_3)e^{-j\omega t}=\delta(x_3-\zeta_3)e^{-j\omega t} \tag{3}$$

In the above equations, U_n is the spatial solution within each region corresponding to excitation at location ζ_n. E, b, and ρ each represent the Young's modulus, damping factor, and density within each region. Assuming time harmonic response allows us to separate time-dependence from (1)-(3).

$$-\omega^2\rho_{si}-(E_{si}-j\omega b_{si})\frac{\partial^2U_1(x_1\mid\zeta_1)}{\partial {x_1}^2}=\delta(x_1-\zeta_1) \tag{4}$$

$$-\omega^2\rho_{diel}-(E_{diel}-j\omega b_{diel})\frac{\partial^2U_2(x_2\mid\zeta_2)}{\partial {x_2}^2}=\delta(x_2-\zeta_2) \tag{5}$$

$$-\omega^2\rho_{si}-(E_{si}-j\omega b_{si})\frac{\partial^2U_3(x_3\mid\zeta_3)}{\partial {x_3}^2}=\delta(x_3-\zeta_3) \tag{6}$$

The general solution in each region is a sum of sine and cosine terms, where k_{diel} and k_{si} are the wavenumbers in region 2 (dielectric) and regions 1 and 3 (resonator body and electrode), respectively.

$$\begin{gathered}U_1(x)=A_1\sin(k_{si}x_1)+B_1\cos(k_{si}x_1)\\U_2(y)=A_2\sin(k_{diel}x_2)+B_2\cos(k_{diel}x_2)\\U_3(z)=A_3\sin(k_{si}x_3)+B_3\cos(k_{si}x_3)\\k_{si}=\frac{\omega}{c_{si}},\ k_{diel}=\frac{\omega}{c_{diel}}\end{gathered} \tag{7}$$

These displacements are then subject to the boundary conditions in (8)-(13) for the impulse on the left dielectric interface for a free resonator.

$$U_1(0)=0 \tag{8}$$

$$\frac{dU_3}{dx_3}(0)=0 \tag{9}$$

$$U_1(L_{body})=U_2(-\frac{g}{2}) \tag{10}$$

$$U_3(-L_{elec})=U_2(\frac{g}{2}) \tag{11}$$

$$E_{diel}\frac{dU_2}{dx_2}\bigg|_{x_2=-g/2}-E_{si}\frac{dU_1}{dx_1}\bigg|_{x_1=L_{body}}=-\frac{\varepsilon_0\varepsilon_rV_{DC}}{g^2} \tag{12}$$

$$E_{si}\frac{dU_3}{dx_3}\bigg|_{x_3=-L_{elec}}-E_{diel}\frac{dU_2}{dx_2}\bigg|_{x_2=g/2}=0 \tag{13}$$

Here, L_{body} and L_{elec} refer to the length of the inner body and the electrode, respectively. For an impulse on the right dielectric interface, (8)-(11) are still valid, but (12)-(13) change to (14)-(15).

$$E_{diel}\frac{dU_2}{dx_2}\bigg|_{x_2=-g/2}-E_{si}\frac{dU_1}{dx_1}\bigg|_{x_1=L_{body}}=0 \tag{14}$$

$$E_{si}\frac{dU_3}{dx_3}\bigg|_{x_3=-L_{elec}}-E_{diel}\frac{dU_2}{dx_2}\bigg|_{x_2=g/2}=\frac{\varepsilon_0\varepsilon_rV_{DC}}{g^2} \tag{15}$$

The results for each excitation are then summed to give the mode shapes in each region. For brevity, only the expression for the mode shape in the inner body is shown below in (16)-(18). In the limiting case where the dielectric film is acoustically matched with the resonator body, this expression simplifies to that given by the theory in [1].

$$A_1=\frac{2\varepsilon_0\varepsilon_rV_{DC}\sin\left(k_{diel}\frac{g}{2}\right)}{g^2}\frac{1}{E_{si}k_{si}}\frac{N_1}{D_1},\quad B_1=0,\quad\text{where} \tag{16}$$

$$N_1=\sqrt{\frac{E_{diel}\rho_{diel}}{E_{si}\rho_{si}}}\sin\left(k_{diel}\frac{g}{2}\right)\cos\left(k_{si}\left(\frac{g}{2}-\frac{L}{2}+d\right)\right)-\cos\left(k_{diel}\frac{g}{2}\right)\sin\left(k_{si}\left(\frac{g}{2}-\frac{L}{2}+d\right)\right) \tag{17}$$

$$D_1=\sin(k_{diel}g)\left[\frac{E_{diel}\rho_{diel}}{E_{si}\rho_{si}}\cos\left(k_{si}\left(\frac{g}{2}-\frac{L}{2}+d\right)\right)\sin\left(k_{si}\left(d-\frac{g}{2}\right)\right)-\sin\left(k_{si}\left(\frac{g}{2}-\frac{L}{2}+d\right)\right)\cos\left(k_{si}\left(d-\frac{g}{2}\right)\right)\right]-\sqrt{\frac{E_{diel}\rho_{diel}}{E_{si}\rho_{si}}}\cos(k_{diel}g)\cos\left(k_{si}\left(\frac{L}{2}-g\right)\right) \tag{18}$$

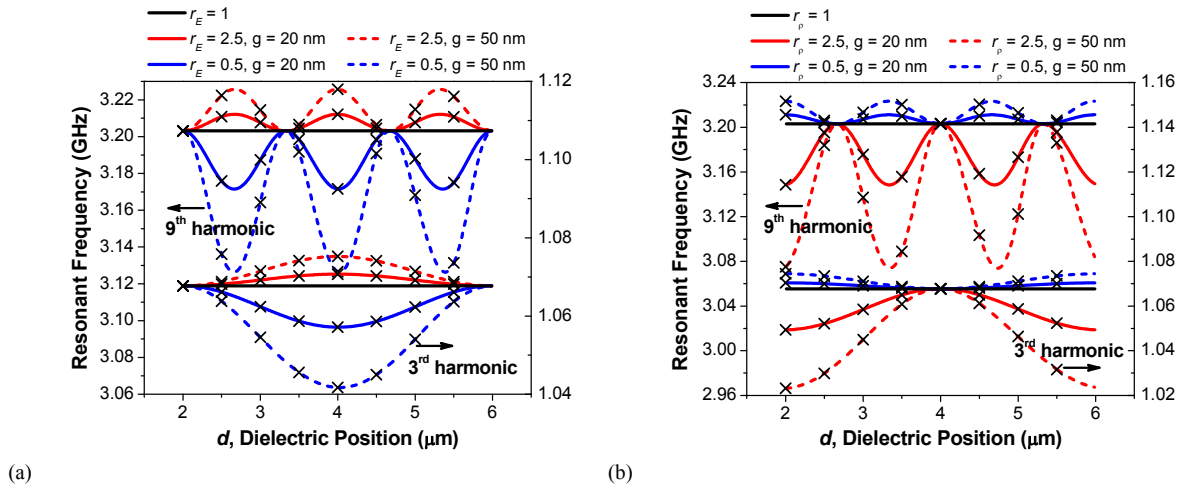

(a) (b)

Figure 2. (a) f_o vs. d with $r_\rho = 1$ and different values of r_E and g for 3rd and 9th harmonic. (b) f_o vs. d with $r_E = 1$ and different values of r_ρ and g for 3rd and 9th harmonic. For both plots, COMSOL simulation results are overlaid in X's.

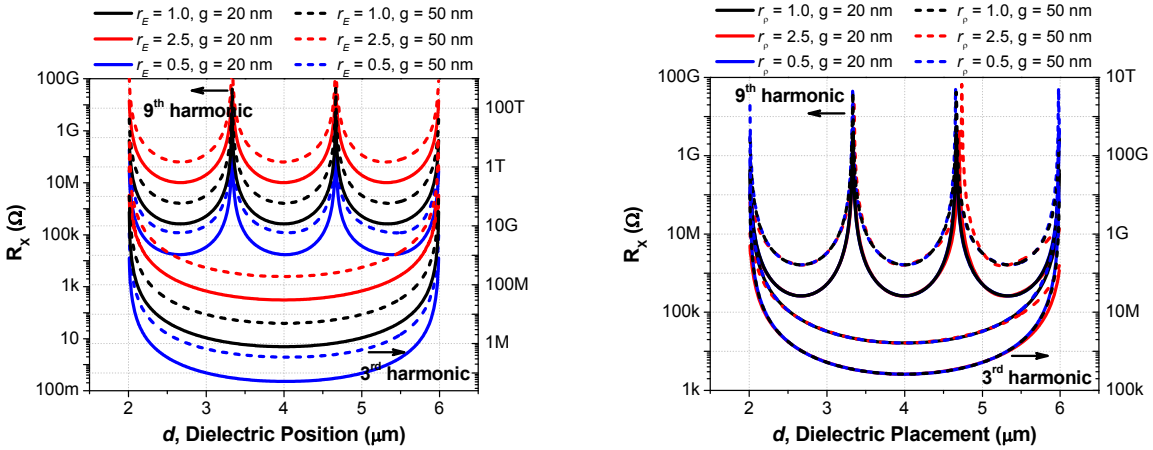

(a) (b)

Figure 3. (a) R_X vs. d with $r_\rho = 1$ and different values of r_E and g for 3rd and 9th harmonic. (b) R_X vs. d with $r_E = 1$ and different values of r_ρ and g for 3rd and 9th harmonic. In the plot, the black and blue plots overlap over almost the entire range.

Similar to (16), if we were to define D_n for all amplitude coefficients in (7), we observe that $D_1 = D_2 = D_3$. We see that solutions to the expression $D_1 = 0$ gives the resonant frequencies of the system.

III. Numerical Simulation Results

Due to the complex nature of the above equations, numerical simulations in MATLAB were used to gain insight into the results of the preceding analysis. For the numerical simulations, we introduce two parameters that characterize the acoustic mismatch between the two materials: r_E and r_ρ, defined as

$$r_E = \sqrt{\frac{E_{diel}}{E_{si}}},\ r_\rho = \sqrt{\frac{\rho_{diel}}{\rho_{si}}}\ . \tag{19}$$

The dependence of the motional impedance and resonant frequency on these parameters are found using simulations on a resonator with L = 12 μm, corresponding to a 3rd harmonic frequency of 1.067 GHz and an acoustic wavelength of 8 μm in a uniform bar resonator.

First, we sweep the resonant frequency as a function of the dielectric position d and parameterize by both r_E and r_ρ, as shown in Fig. 2. COMSOL simulation results are also included in these plots and show good agreement with the presented theory. We see from both these plots that the dependence on d is roughly sinusoidal with a wavelength equal to half that of the resonant wavelength in the resonator body. The average value and amplitude of the sinusoid is dependent upon r_E, r_ρ, and g. For $r_E > 1$ or $r_\rho < 1$, we see the resonant frequency increase. This is expected since the

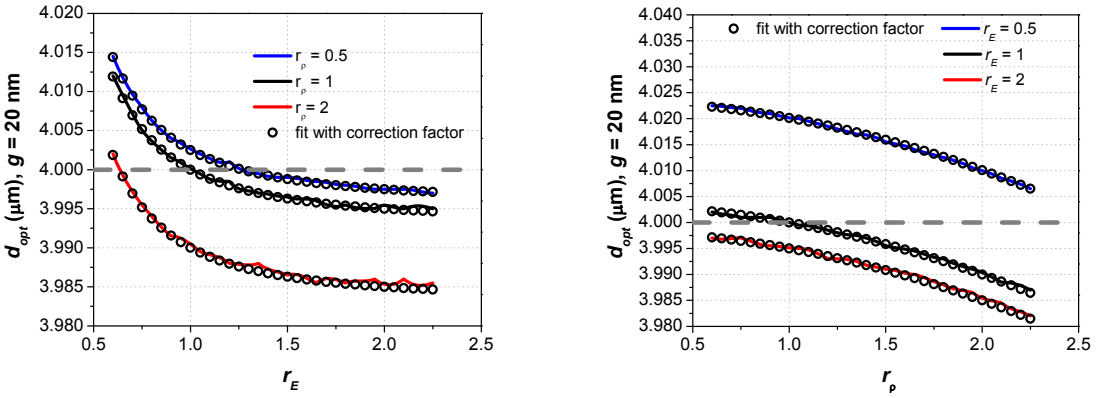

(a) (b)

Figure 4. (a) d_{opt} vs. r_E with g = 20 nm for different values of $r_ρ$ at 3rd harmonic. (b) d_{opt} vs. $r_ρ$ with g = 20 nm for different values of r_E at 3rd harmonic. The dotted grey line shows the optimal dielectric position for acoustically matched layers.

resonator is effectively becoming stiffer or lighter. The opposite is true for $r_E < 1$ or $r_ρ > 1$. Also, as g increases, a larger portion of the resonator is affected by the acoustic mismatch, which explains the increase in frequency deviation with g.

Close inspection of Fig. 2(a) and (b) shows that at displacement nodes, the frequency varies minimally with $r_ρ$ and maximally with r_E. The opposite is also true at displacement maxima. This intuitively suggests that the dielectric film acts as a mass-spring system that couples the inner body and the electrode of the resonator.

A mechanical resonator can be modeled as a distributed network of infinitesimal masses and springs, just like a transmission line is modeled as a network of infinitesimal inductances and capacitances. Since we are assuming that g is much smaller than the acoustic wavelength in the dielectric film λ_{diel} (i.e., low-GHz frequencies), we can model this whole system as two transmission lines representing the inner body and the electrode coupled by a mass-spring element, which represents the dielectric film.

This observation helps make sense of the numerical simulation results. At displacement nodes, the coupling mass does not contribute much since it does not move, while the coupling spring contribution is large since it is stretched maximally (i.e., maximum strain). On the other hand, at displacement maxima, the strain is minimal so the coupling spring contribution is small while the coupling mass contributes largely since it moves maximally. Note that this is only valid when the thickness of the dielectric film g is small compared to the acoustic wavelength of the dielectric film.

Next, the motional impedance as a function of d and parameterized by both r_E and $r_ρ$ is plotted in Fig. 3. We define the motional impedance as $R_x = v_{in}/i_{out}$ where small values indicate efficient transduction. Fig. 3 shows results similar to those described in [1]. However, closer examination shows that the minimum point of motional impedance shifts according to r_E and $r_ρ$. The primary reason for this is due to the distortion of the mode shape. The same intuition developed in [1] is still valid, namely that the center of the dielectric film should be at a displacement node; the only difference is that the displacement node is now shifted to a slightly different point. Having verified this claim, the remainder of this paper will focus on resonator behavior when the dielectric film is placed close to the optimal position.

Fig. 3 reveals that the minimum motional impedance is a strong function of r_E but remains roughly constant with $r_ρ$. In fact, we see that the minimum motional impedance shows a roughly quartic dependence on r_E. Inspection of the magnitude of (17) and (18) via numerical simulation shows that N_1 is roughly proportional to $r_ρ/r_E$ while D_1 is roughly proportional to $r_ρ r_E$. Thus, the $r_ρ$ factor cancels out and the resonant amplitude becomes proportional to r_E^{-2}. Since the output displacement current is proportional to the square of the resonant amplitude, the overall proportionality of the motional impedance becomes r_E^4.

Finally, numerical simulations are used to find the shift in the optimal dielectric position (d_{opt}) as a function of r_E and $r_ρ$. Fig. 4 shows these simulation results for different dielectric film thicknesses. With some simplification, we can find an analytical expression to estimate the shift in optimal dielectric position,

$$\frac{d_{opt,new}}{d_{opt}} = \frac{1-\frac{g}{L}}{1-\frac{g}{L}\frac{E_{si}}{E_{diel}}} \frac{1-\frac{g}{2L}\frac{\rho_{diel}}{\rho_{si}}}{1-\frac{g}{2L}}. \quad (20)$$

The estimated fit using (20) is shown in Fig. 4 and shows good agreement with the simulated results. Note that roughness in the simulation results is due to resolution limits in the numerical simulation and improve with better frequency and spatial resolution in the simulation at the cost of simulation time.

As a check, numerical simulations were also conducted on resonators using common dielectric materials such as silicon nitride and hafnium oxide. These results are shown below in Fig. 5. Table 1 lists the minimum motional impedances for different dielectric films and resonator geometries. Here we

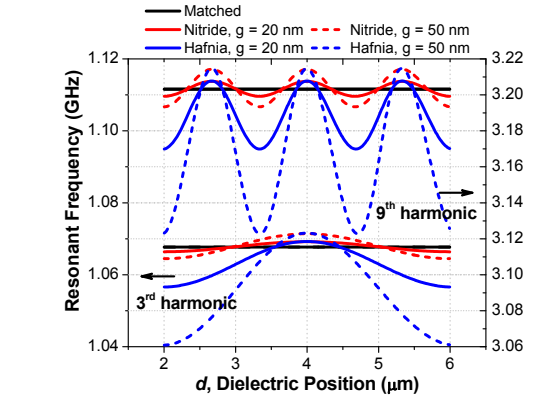

(a)

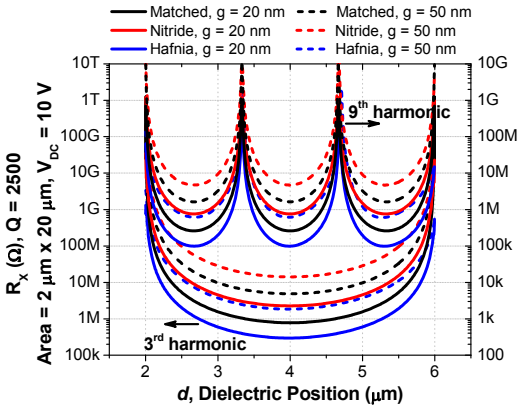

(b)

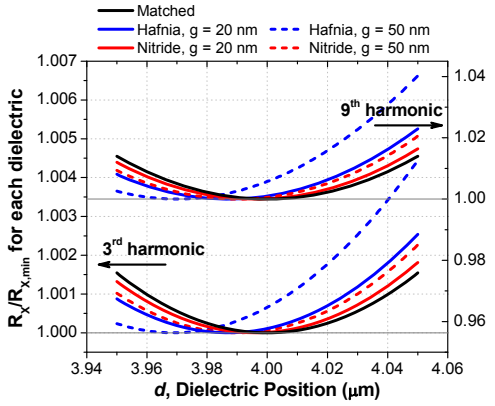

(c)

Figure 5. (a) f_o vs. d with for different values of g and dielectric materials at 3rd and 9th harmonic. (b) R_X vs. d with for different values of g and dielectric materials at 3rd and 9th harmonic. (c) Close-up view of normalized R_X for different dielectric materials.

see the significance of the quartic dependence of motional impedance on r_E. Although silicon nitride has a dielectric constant roughly twice as large as oxide, its use results in a much higher motional impedance because it is extremely stiff. Using hafnia results in a lower impedance than what is obtained using oxide, but not nearly as low as expected if taking into account only the improvement due to higher dielectric constant. This indicates that the material stiffness

TABLE I. 3RD HARMONIC MOTIONAL IMPEDANCES FOR VARIOUS DIELECTRIC MATERIALS

Dielectric	g	d_{opt}	$R_{x,min}$
Acoustically Matched $\varepsilon_{diel} = 7$, $E_{diel} = 170$ GPa, $\rho_{diel} = 2330$ kg/m^3	20 nm	4 μm	781 kΩ
	50 nm	4 μm	4.88 MΩ
Nitride $\varepsilon_{diel} = 7$, $E_{diel} = 290$ GPa, $\rho_{diel} = 3184$ kg/m^3	20 nm	3.997 μm	2.27 MΩ
	50 nm	3.991 μm	14.1 MΩ
Hafnia $\varepsilon_{diel} = 20$, $E_{diel} = 300$ GPa, $\rho_{diel} = 9680$ kg/m^3	20 nm	3.988 μm	297 kΩ
	50 nm	3.968 μm	1.85 MΩ
Oxide $\varepsilon_{diel} = 4$, $E_{diel} = 66$ GPa, $\rho_{diel} = 2270$ kg/m^3	20 nm	4.009 μm	367 kΩ
	50 nm	4.026 μm	2.36 MΩ

along with the dielectric constant must be considered in choosing the optimal dielectric material.

IV. CORRECTION FACTORS

Using energy methods and applying simplifying assumptions, we are able to find a correction to the resonant frequency given by (21).

$$\frac{f_{o,new}}{f_o} = \frac{1-\frac{2g}{L}\frac{E_{si}}{E_{diel}}\cos^2\left(\frac{n\pi d}{L}\right)}{1-\frac{2g}{L}\cos^2\left(\frac{n\pi d}{L}\right)} \frac{1-\frac{2g}{L}\sin^2\left(\frac{n\pi d}{L}\right)}{1-\frac{2g}{L}\frac{\rho_{diel}}{\rho_{si}}\sin^2\left(\frac{n\pi d}{L}\right)} \quad (21)$$

For optimal resonator design, the dielectric placement is at a displacement node, meaning that the second factor in (21) becomes almost unity. Thus, we see that for an optimally designed resonator, the density mismatch contributes negligibly to the resonant frequency shift. On the other hand, the mismatch in the Young's moduli significantly affects the correction factor in (21) for an optimally designed resonator. This matches well with what is observed from numerical simulations. Similarly, a correction to the motional impedance can be given by

$$R_{x,new} = \left(\frac{E_{diel}}{E_{si}}\right)^2 R_x \,. \quad (22)$$

Finally, we verify the accuracy of these correction factors by plotting the resonant frequency and motional impedance as a function of r_E for various values of dielectric thickness g in Fig. 6. The dielectric is optimally placed for all plotted results. The results are not plotted with respect to r_ρ since it contributes negligibly in this case. Overlaid on the plots are the estimated values for each case using the correction factors in (21) and (22). Figure 6(c) and (d) plot the error in correction factor for both the resonant frequency and motional impedance. We see a maximum frequency error of approximately 1300 ppm and a maximum motional

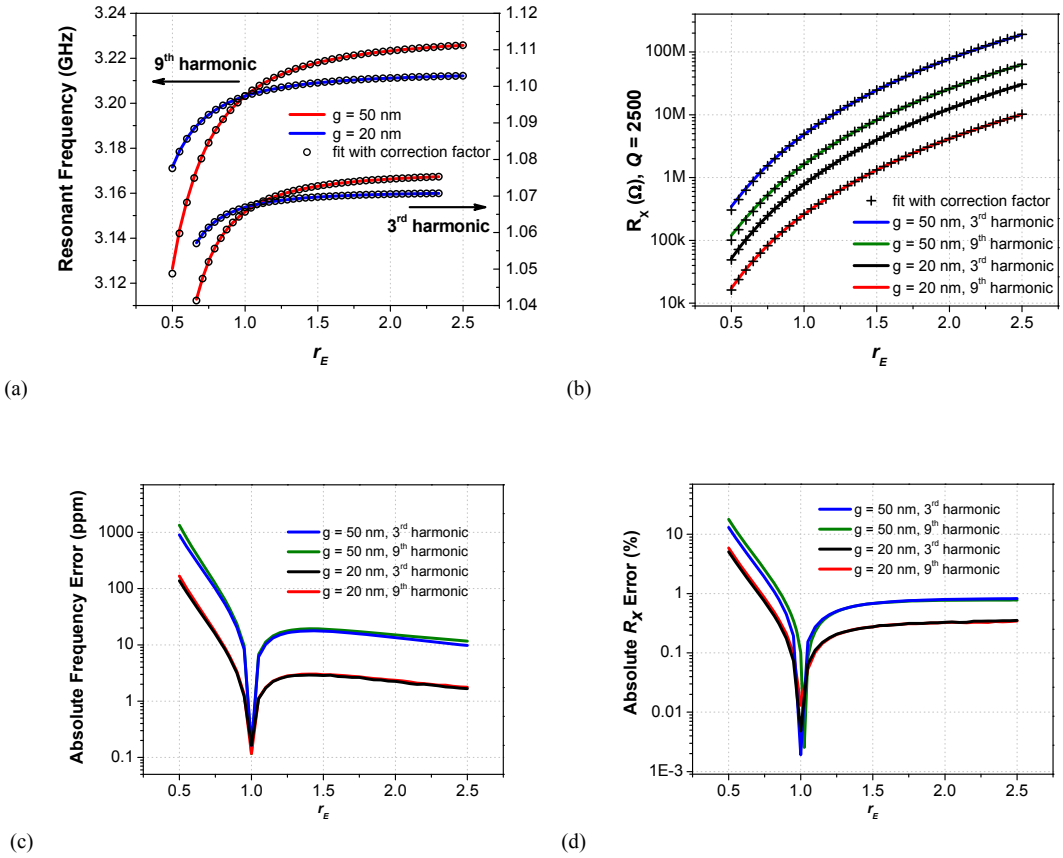

Figure 6. (a) f_o vs. r_E for different values of g at 3rd and 9th harmonic. (b) R_x vs. r_E for different values of g at 3rd and 9th harmonic. (c) Percent frequency error between simulated resonant frequency and that estimated by (21). (d) Percent R_x error between simulated motional impedance and that estimated by (22).

impedance error of approximately 18%. These maximum errors occur for the lowest plotted values of r_E and decrease steadily until r_E = 1, where they approach zero. The frequency resolution used for this simulation is 100 Hz. We can see that the error is heavily dependent upon g, which can be attributed to the assumptions used to simplify (21) and (22), specifically that $g << \lambda_{diel}$.

V. Conclusions

In summary, this paper presents a supplement to the theory presented in [1] for internal dielectrically transduced micromechanical resonators that includes the effects of acoustic mismatch on resonator performance. This paper also provides correction factors to provide a precise set of design equations. The intuition provided in this paper indicates that for optimally designed resonators, to first order, only the mismatch in the Young's moduli affects the properties of the resonator. Although the exact theory in this paper is specific to a bar resonator, this insight can be extended to any similar composite bulk-mode resonator. Also, we have highlighted the importance of the Young's moduli mismatch in selecting dielectric materials for optimal transduction efficiency. These insights should help designers optimize designs for internal dielectrically transduced micromechanical resonators for use in larger systems.

References

[1] D. Weinstein and S. A. Bhave, "Internal dielectric transduction: optimal position and frequency scaling," *IEEE Transactions on Ultrasonics, Ferroelectrics, and Frequency Control*, vol. 54, no. 12, pp. 2696-98, Dec. 2007.

[2] S.-S. Li, Y.-W. Lin, Z. Ren, C. T.-C. Nguyen, "An MSI micromechanical differential disk-array filter," *IEEE International Conference on Solid-State Sensors, Actuators, and Microsystems (Transducers 2007)*, June 10-14, 2007, pp. 307-311.

[3] G. Piazza, P. J. Stephanou, A. P. Pisano, "Piezoelectric aluminum nitride vibrating contour-mode MEMS resonators," *IEEE/ASME Journal of Microelectromechanical Systems*, vol. 15, no. 6, pp. 1406-1418, Dec. 2006.

[4] D. Weinstein, S. A. Bhave, S. Morita, S. Mitarai, K. Ikeda, "Frequency scaling and transducer efficiency in internal dielectrically transduced silicon bar resonators," *IEEE International Conference on Solid-State Sensors, Actuators, and Microsystems (Transducers 2009)*, June 21-25, 2009, pp. 708-711.

[5] Y.-W. Lin, S.-S. Li, Y. Xie, Z. Ren, C. T.-C. Nguyen, "Vibrating micromechanical resonators with solid dielectric capacitive transducer gaps," *IEEE International Frequency Control Symposium (FCS 2005)*, August 29-31, 2005, pp. 128-134.

[6] M. Ziaei-Moayyed, D. Elata, J. Hsieh, J.-W. P. Chen, E. P. Quévy, R. T. Howe, "Fully differential internal electrostatic transduction of a lamé-mode resonator," *IEEE International Conference on Micro Electro Mechanical Systems (MEMS 2009)*, January 25-29, 2009, pp. 931-934.

[7] V. Kaajakari, A. T. Alastalo, T. Mattila, "Electrostatic transducers for micromechanical resonators: free space and solid dielectric," *IEEE Transactions on Ultrasonics, Ferroelectrics, and Frequency Control*, vol. 53, no. 12, pp. 2484-2489, Dec. 2006.

[8] K. F. Graff, *Wave Motion in Elastic Solids*. New York: Dover, 1975.